Mon. Not. R. Astron. Soc. **324**, 141–148 (2001)

Particle-mesh simulations of the Lyα forest

Avery Meiksin[1]★ and Martin White[2]
[1]*Institute for Astronomy, University of Edinburgh, Blackford Hill, Edinburgh EH9 3HJ*
[2]*Astronomy Department, Harvard University, 60 Garden Street, Cambridge, MA 02138, USA*

Accepted 2000 December 7. Received 2000 December 7; in original form 2000 August 23

ABSTRACT

Numerical hydrodynamical simulations have proven to be a successful means of reproducing many of the statistical properties of the Lyα forest as measured in high-redshift quasar spectra. Pseudo-hydrodynamical methods, based only on simulating the dark matter component, have been claimed to yield a comparable level of success. We investigate the degree to which two pseudo-methods, with and without allowing for a pseudo-gas pressure, are able to match the predictions of fully hydrodynamical plus dark matter simulations. We also address the requirements for convergence to the statistics of the spectra and the inferred properties of the Lyα forest as a function of resolution and box size. Generally, we find that it is possible to reach agreement with full hydrodynamic simulations at the 10 per cent level in the cumulative distributions of the flux and absorption line parameter statistics for readily achievable particle and grid numbers, but difficult to do much better.

Key words: methods: numerical – intergalactic medium – quasars: absorption lines.

1 INTRODUCTION

Numerical simulations of structure formation in the Universe incorporating hydrodynamics in cold dark matter (CDM) dominated cosmologies have proven very successful in reproducing the statistical properties of the Lyα forest as measured in high-redshift quasi-stellar object (QSO) spectra (Cen et al. 1994; Zhang, Anninos & Norman 1995; Hernquist et al. 1996; Bond & Wadsley 1997; Zhang et al. 1997; Theuns, Leonard & Efstathiou 1998a). The high level of statistical agreement suggests that the models capture the essential physical nature of the absorbing structures (Meiksin et al. 2001). Much of the structure of the intergalactic medium (IGM) may be understood as a consequence of the spatial coherence in the statistical properties of the density fluctuations of the dark matter alone in a 'cosmic web', as emphasized by Bond & Wadsley and supported by the slow comoving evolution of the integalactic filaments found by Zhang et al. (1998). Gnedin & Hui (1998) claim that, in fact, it is unnecessary to incorporate full hydrodynamics in the simulations to reproduce the properties of the Lyα forest. Gnedin & Hui introduce a pseudo-hydrodynamical scheme into an *N*-body calculation instead, reporting comparable results in the distributions of flux and H I column density to full hydrodynamical + *N*-body simulations for a standard CDM model. Pseudo-hydrodynamical methods based on the particle-mesh (PM) technique alone have been used by Petitjean, Mücket & Kates (1995) and Croft et al. (1998).

Because of the large computational overhead in incorporating proper hydrodynamics into an *N*-body code, considerable benefit would be obtained if the hydrodynamics computations could be avoided. It would then be possible to perform a wide range of cosmological models at only moderate computational expense, as well as test systematics on the properties of the forest: the effect of box size, resolution, and even physical effects like variations in the character of the background UV radiation field that ionizes the gas. It would be of additional theoretical interest to infer the degree to which the properties of the forest are hydrodynamical in origin, as opposed to being solely a consequence of the clustering of dark matter.

To these ends, we perform simulations of the Lyα forest for a variety of cosmological models using two approaches: a pure gravitational computation using a PM *N*-body code (PM simulations), and a pseudo-hydrodynamical technique, based on the method of Gnedin & Hui, incorporating an effective gas pressure force computed from the local dark matter density (HPM simulations).

2 THE MODELS AND SIMULATIONS

We consider two sets of models. The first is based on simulations in a flat CDM model with a cosmological constant (ΛCDM) using both the PM and HPM codes. These are performed in order to test convergence of the results for differing box sizes, particle numbers, and grid resolutions. A second set is based on four CDM models in Machacek et al. (2000, hereafter M00), who performed computations using full hydrodynamics. We duplicate their models in order to compare our resulting statistics for the absorption features with theirs. The models investigated, in addition to the ΛCDM model, are: a standard critical-density flat CDM model without a cosmological constant (SCDM), an open CDM model (OCDM),

★ E-mail: A.Meiksin@roe.ac.uk

Table 1. Parameters for the cosmological models. Ω_0 is the total mass density parameter, Ω_Λ the cosmological constant density parameter, Ω_b the baryonic mass fraction, $h = H_0/100\,\mathrm{km\,s^{-1}\,Mpc^{-1}}$, where H_0 is the Hubble constant at $z = 0$, n the slope of the primordial density perturbation power spectrum, and $\sigma_{8\,h^{-1}}$ the fluctuation normalization in a sphere of radius $8\,h^{-1}\,\mathrm{Mpc}$.

Model	Ω_0	Ω_Λ	Ω_b	h	n	$\sigma_{8\,h^{-1}}$
ΛCDM	0.4	0.6	0.0355	0.65	1	1.0
OCDM	0.4	0	0.0355	0.65	1	1.0
SCDM	1	0	0.06	0.5	1	0.7
tCDM	1	0	0.07	0.6	0.81	0.5

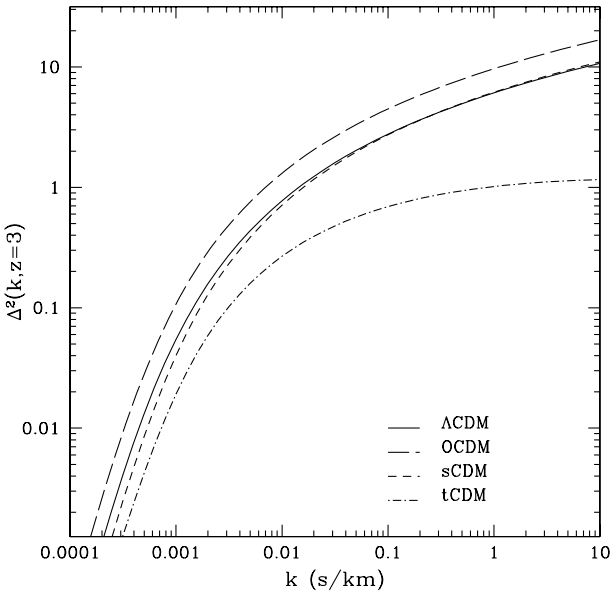

Figure 1. Non-dimensional linear power spectra $\Delta^2(k) = k^3P(k)/2\pi^2$, where $P(k)$ is the power spectrum, for the four cosmological models examined. Shown at $z = 3$.

and the standard CDM model but with the power spectrum of the density perturbations tilted (tCDM) to match the normalization on large scales as determined from the *COBE* measurements of the cosmic microwave background (Bunn & White 1997). The model parameters are shown in Table 1. As in M00, the initial data were generated using the BBKS transfer function (Bardeen et al. 1986) to compute the starting redshifts and the unconstrained initial particle positions and velocity perturbations appropriate for each model. The non-dimensional linear power spectra $\Delta^2(k)$ are shown at $z = 3$ in Fig. 1.

To account for the degree of ionization of hydrogen, it is also necessary to include a background UV radiation field. We essentially circumvent this by fixing the mean optical depth, as defined by $\bar{\tau}_\alpha = -\log\langle\mathrm{flux}\rangle$, at $\bar{\tau}_\alpha = 0.30$ at $z = 3$, as in M00.

The evolution is computed using the PM code described in detail in Meiksin, White & Peacock (1999) and White (1999). The computational volume is chosen to be periodic with a side length of 1, and we take as our time coordinate the logarithm of the scale factor, $\log a$, where $a \equiv (1+z)^{-1}$. Velocities are measured in units of the expansion velocity across the box aHL_{box}, where H is the Hubble parameter fixed by the Friedmann equation

$$H^2 \equiv H_0^2\left(\frac{\Omega_{\mathrm{mat}}}{a^3} + \Omega_\Lambda + \frac{\Omega_K}{a^2}\right) \tag{1}$$

Table 2. Physical parameters for the PM simulations. L is the comoving box size in units of $h^{-1}\,\mathrm{Mpc}$. Also shown is the dimensionless linear power spectrum $\Delta^2(2\pi/L)$ at $z = 3$. The number of dark matter particles used is N_{p}^3 and the number of grid zones for the force calculation is N_{g}^3.

Model	$L\ (h^{-1}\,\mathrm{Mpc})$	$\Delta^2(2\pi/L)$	N_{p}	N_{g}
ΛCDM	6.24	0.64	256	256
ΛCDM	9.6	0.45	128	256
ΛCDM	9.6	0.45	256	256
ΛCDM	9.6	0.45	256	512
ΛCDM	12.48	0.35	256	512
OCDM	6.24	0.98	256	256
SCDM	4.8	0.50	256	256
tCDM	5.76	0.19	256	256

in terms of the Hubble constant H_0 and the densities in matter, cosmological constant and curvature, in units of the critical density. The density is defined from the particle positions by assigning particles to a regular Cartesian grid using the cloud-in-cell (CIC) scheme (Hockney & Eastwood 1988). The Fourier transform is taken and the force computed using the kernel $\boldsymbol{k}/k^2$. We use a second-order leap frog method to integrate the equations. The relevant positions are predicted at a half time step and used to calculate the accelerations which modify the velocities. The time step is dynamically chosen as a small fraction of the free-fall time with a maximum size of $\Delta \log a = 3$ per cent.

The initial conditions were created by displacing the particles from a uniform grid using the Zel'dovich approximation.

Our implementation of the HPM code differs slightly from that in Gnedin & Hui (1998). First, we use two sets of particles, one of which feels only the gravitational force (the 'dark matter') and the other of which additionally feels a pseudo-pressure force (the 'gas'). The gravity is computed as before. To compute the 'hydro' forces we bin the 'gas' particles on to a grid using CIC as for the gravity. We compute the temperature using the equation of state

$$T = T_0\left(\frac{\rho}{\bar{\rho}}\right)^{\gamma-1}, \tag{2}$$

where T_0 and γ are obtained from Hui & Gnedin (1997), assuming a reionization redshift of $z_{\mathrm{ri}} = 6$, as in M00. The enthalpy per particle

$$\varphi = \frac{\gamma}{\gamma-1}T \tag{3}$$

is then computed, Fourier transformed and smoothed by a Gaussian of half a grid cell (to suppress high-frequency noise). The 'hydro' force is then calculated from the inverse Fourier transform of $\mathrm{i}\boldsymbol{k}\tilde{\varphi}$ and added to the gravitational force for the 'gas' particles.

In practice, T_0 and γ will depend on the reionization history of the IGM. In particular, if He II is reionized (to He III) late, lower values of T_0 will result prior to He II reionization and higher values in rarified gas after (Meiksin 1994). The effect of reionization on the thermal properties of the gas will only be known once the nature of the ionizing sources has been established, and may eventually require the incorporation of radiative transfer into the simulations.

We consider a variety of particle number and grid zone combinations, as well as several box sizes. The PM simulations are summarized in Table 2. For the HPM simulations, two combinations are used: $(N_{\mathrm{p}}, N_{\mathrm{g}}) = (128, 256)$ and $(256, 512)$. For HPM, the dark matter and the gas are represented by an identical number of particles, each equal to N_{p}^3.

Given a set of final particle positions and velocities, we compute the spectra as follows. First, the density and density-weighted line-of-sight velocity are computed on a grid (using CIC interpolation as above) and Gaussian smoothed using fast Fourier transform (FFT) techniques in order to sample the velocity field adequately. This forms the fundamental data set. A grid of sightlines is drawn through the box, parallel to the box sides, and along each sightline a new 1D grid of density and velocity is obtained from the fundamental grid using CIC interpolation. The position in velocity units and the temperature are computed on this 1D grid using the cosmological model and equation (2) for the equation of state.

Using this 1D grid we then integrate in real space to find $\tau(u)$ at a given velocity u. Specifically, we define

$$\tau(u) = A \int \mathrm{d}x \left[\frac{\rho(x)}{\bar{\rho}}\right]^2 T(x)^{-0.7} b^{-1} \exp[-(u-u_0)^2/b^2], \qquad (4)$$

where $u_0 = xaHL_{\rm box} + v_{\rm los}$ and $b = \sqrt{2k_{\rm B}T/m_{\rm H}}$ is the Doppler parameter, where $m_{\rm H}$ is the mass of a hydrogen atom. The flux at velocity u is $\exp(-\tau)$. The integration variable x indicates the distance along the box in terms of the expansion velocity across the box. The constant A is then iteratively adjusted to obtain a predefined $\bar{\tau}_\alpha = -\log\langle\exp(-\tau)\rangle$.

We generate sample spectra from the simulated data along random lines-of-sight through the computational boxes over the length of each box. In order to make a fair comparison with the data in M00, both sets of spectra are rebinned to a constant pixel resolution of $\lambda/\Delta\lambda = 74\,000$ and Gaussian smoothed to mimic a spectral resolution of $8\,\mathrm{km\,s^{-1}}$. These parameters were chosen to approximate what may be achieved using the Keck HIRES.

There are several measurements of the Lyα forest which may be used as a basis for comparison. The most fundamental is simply the distribution of flux per pixel in the synthesized spectra. The fluctuations in the flux on different velocity scales provide additional constraints, which may be related both to the density fluctuation power spectrum and to the thermal widths of the lines. We quantify the fluctuations in three ways. We compute the power spectrum $P_{\rm F}(k)$ of the flux, an analogue of the density power spectrum. (For the $P_{\rm F}(k)$ estimates we use the raw spectra from the PM and HPM runs.) The widths of the spectral features may be directly characterized using wavelets, which quantify the changes in a given spectrum on being smoothed from one velocity resolution to another (Meiksin 2000). A multiscale analysis based on the Daubechies wavelets effectively performs a weighted smoothing of the spectrum over successive doublings of the pixel width. We use a Daubechies wavelet of order 20. Lastly, the most traditional method to quantify the flux fluctuations is by decomposing each spectrum into a set of Voigt line profiles. We utilize AUTOVP (Davé et al. 1997) to perform such an analysis. Each sample spectrum produces an average of the order of 900 lines per unit redshift. Typically, $(3\text{–}6)\times10^4$ lines are analysed per model. The absorption lines are characterized by their H I column densities and Doppler parameters. The H I column densities reflect both the density and physical thickness of the structures that give rise to the absorption features. The Doppler parameters reflect the degree of line broadening due both to the thermal motion of atoms and to any internal peculiar velocities within the structures, and may provide probes for the temperature and velocity history of the universe at high redshifts.

To ensure that our results are not affected by sample variance, we performed two independent simulations of some of the models. We found that convergence on the statistical properties could be achieved with a single realization provided the statistics were averaged over a sufficient number of lines-of-sight. We found 3072 lines-of-sight (each one box side in length) was adequate for the PM simulations, and 1024 for HPM.

3 CONVERGENCE TESTS

Simulations of the Lyα forest are restricted by two size constraints. High spatial resolution is required to resolve the structure of the absorbers, while a large box size is required both to capture the large-scale power which will affect the velocity widths of the absorption lines, and to obtain a fair sample of the universe. A small box may be adequate to resolve the line structure; if the box is too small the fluctuations corresponding to the scale of the box will become non-linear, in which case the results are no longer representative of the simulated cosmological model.

Resolution effects were previously studied using full hydrodynamics by Theuns et al. (1998b) and Bryan et al. (1999). Using P^{3}M-SPH, Theuns et al. found for SCDM that a (comoving) box size of at least $2.2\,h^{-1}\,$Mpc using 64^3 SPH particles and 64^3 dark matter particles is required to converge on $\bar{\tau}_\alpha$ and the Doppler parameter distributions at $z = 3$. This corresponds to a mean proper interparticle separation of $11\,h^{-1}\,$kpc, or about half of this in structures with an overdensity of 10, typical of the filaments with H I column densities of 10^{14}–$10^{15}\,\mathrm{cm^{-2}}$ (Zhang et al. 1998). Bryan et al. found that a box size of at least $4.8\,h^{-1}\,$Mpc was needed to reach convergence on the Doppler parameter distribution at $z = 3$ using a PM-PPM code (Kronus) with 128^3 grid cells, corresponding to a proper resolution of $9\,h^{-1}\,$kpc.

Neither group was able to maintain a resolution of $5\,h^{-1}\,$kpc while increasing box sizes beyond $2.4\,h^{-1}\,$Mpc due to memory limitations, so that the contribution of larger scale power at high resolution was left unexplored. We also note that SCDM has less large-scale power than more viable cosmological models like ΛCDM, so that the resolution limitations are least restrictive for SCDM. It is possible to achieve a much higher resolution using PM or HPM. In this section, we present the results of a series of tests of the convergence of the PM and HPM simulations for ΛCDM as the box size, particle number, and number of grid zones are varied. The simulation results are all shown at $z = 3$.

3.1 Flux distribution

A comparison of the cumulative distributions of flux per pixel for several resolutions and box sizes is shown in Fig. 2. The PM-generated distributions agree at low flux values (high optical depths), but diverge for fluxes above 0.8, with differences in the cumulative distributions as large as 0.05. As the resolution of the $9.6\,h^{-1}\,$Mpc box is increased to $(N_{\rm p}, N_{\rm g}) = (256, 512)$, the amount of fine-scale structure continues to increase. The HPM-generated flux distributions differ markedly from the PM results, showing a smaller amount of fine-scale structure. The corresponding flux power spectra $P_{\rm F}(k)$ are show in Fig. 3. Again, as the grid resolution is increased in the $9.6\,h^{-1}\,$Mpc box, the amount of large-scale power continues to increase, while there is a decrease in the amount of power at shorter scales [$k > 0.04\ (\mathrm{km\,s^{-1}})^{-1}$]. The $9.6\,h^{-1}\,$Mpc HPM simulation shows a steepening in power compared with the $9.6\,h^{-1}\,$Mpc PM simulations for $k > 0.05\ (\mathrm{km\,s^{-1}})^{-1}$, suggesting that the gas pressure forces have slightly suppressed power on these scales.

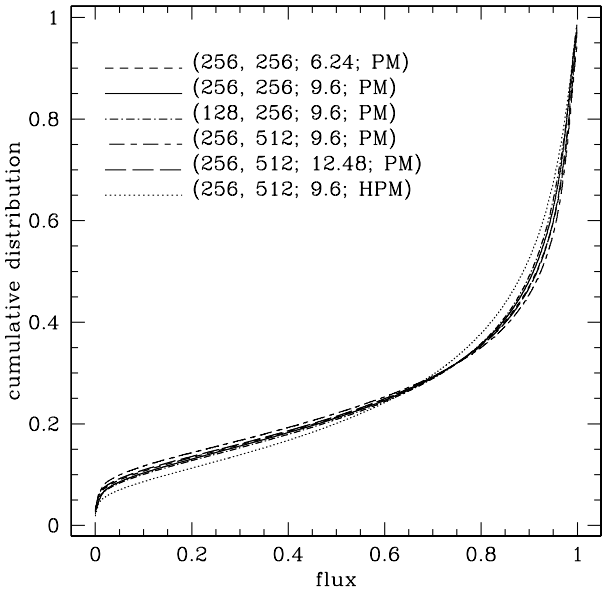

Figure 2. Comparison of cumulative distributions of flux per pixel for the ΛCDM simulations for three different resolutions and three box sizes. The notation for each model is (N_p, N_g; box size; method), where the number of dark matter particles is N_p^3, the number of grid zones is N_g^3, and the box size is in units of h^{-1} Mpc. For the HPM simulations, the numbers of gas and dark matter particles are each N_p^3. The distributions diverge at high flux values (small optical depths), suggesting small structures have not been resolved at the lower resolutions.

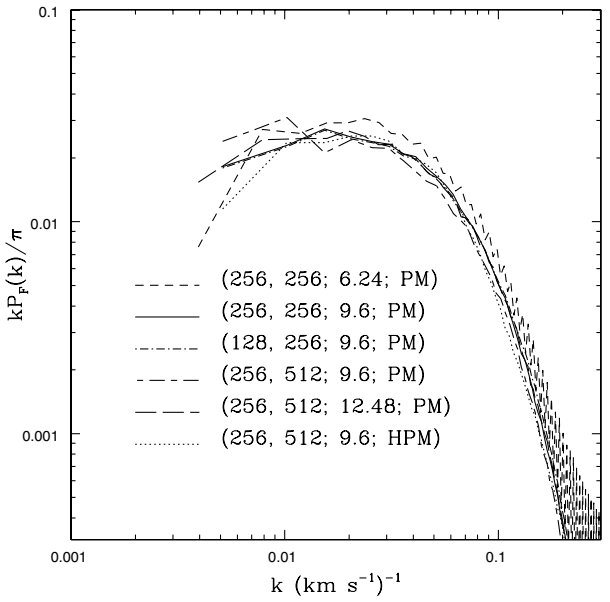

Figure 3. Comparison of flux $P_F(k)$ for the ΛCDM simulations for three grid resolutions and three box sizes. The notation for each model is as in Fig. 2. A larger amount of power is produced in the smallest box simulation compared with the others.

3.2 Wavelet decomposition

The cumulative distributions of wavelet coefficients are shown in Fig. 4. The groups of curve from left to right correspond to the respective velocity scales 4–8, 8–16, 16–32, 32–64 and 64–128 km s^{-1}. The small coefficients at the lowest scales show

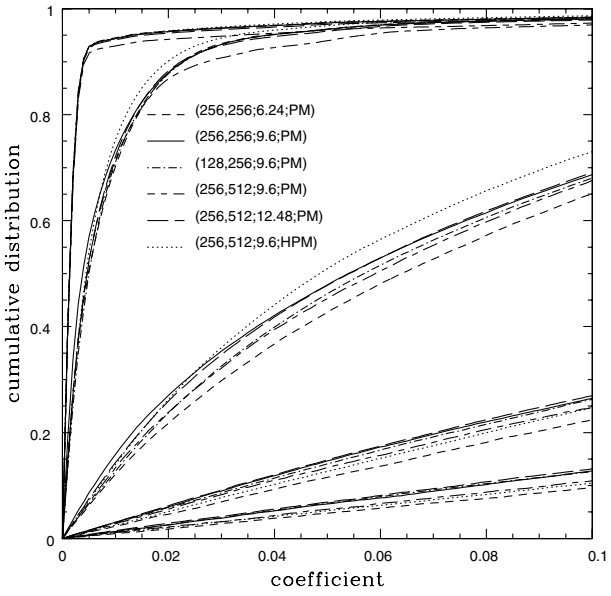

Figure 4. Comparison of wavelet coefficient distributions for the ΛCDM simulations for three resolutions and three box sizes.

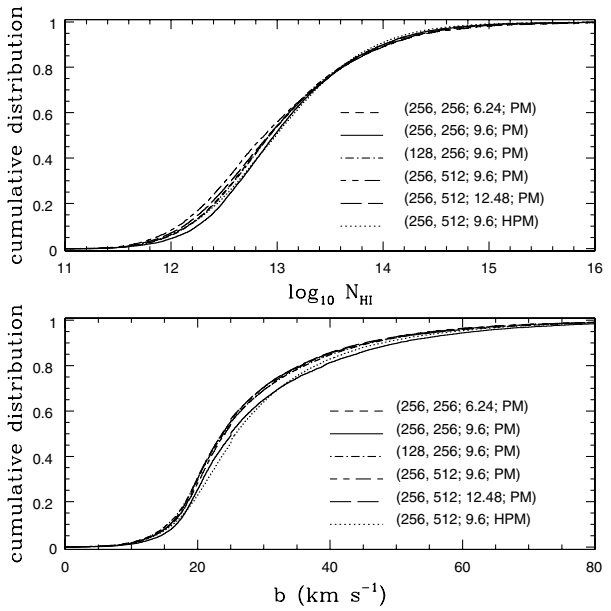

Figure 5. Comparison of cumulative distributions of absorption line parameters for the ΛCDM simulations for three resolutions and three box sizes.

that no features are present on these scales. The physically most interesting scales are represented by the 16–32 km s^{-1} curves, corresponding to typical velocity widths of the absorption lines. The largest differences between the simulations are found on these scales. The convergence for the $9.6\,h^{-1}$ Mpc box simulations is non-monotonic with N_p and N_g, with the $(N_p, N_g) = (128, 256)$ and $(256, 512)$ simulations agreeing well, but not with the $(256, 256)$ simulation. The latter, however, agrees closely with the $(256, 512)$ $12.48\,h^{-1}$ Mpc simulation, suggesting that convergence has been reached with box size. The largest coefficients are found for the smallest box ($6.24\,h^{-1}$ Mpc) simulation, indicating a greater amount of structure in the spectra on these velocity scales

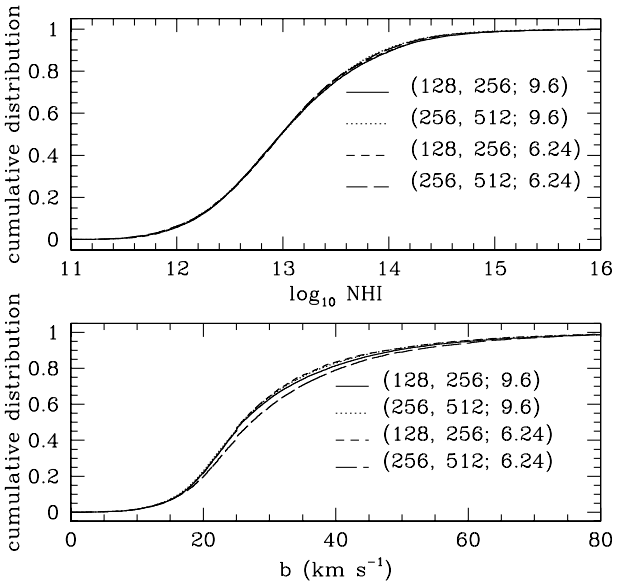

Figure 6. Comparison of cumulative distributions of absorption line parameters for the HPM ΛCDM simulations for two grid resolutions and two box sizes, showing good convergence.

than found for the larger boxes. By contrast, the HPM simulation shows the least amount of structure on these scales.

3.3 Line parameter decomposition

A comparison of the cumulative distributions of $N_{\rm H\,I}$ and b determined by AUTOVP is shown in Fig. 5 for PM simulations for three different pairs of $N_{\rm p}$ and $N_{\rm g}$ and three box sizes. As was found for the wavelet coefficient distributions, the behaviours for both the $N_{\rm H\,I}$ and b distributions are non-monotonic. The $(N_{\rm p}, N_{\rm g}) = (128, 256)$ and $(256, 512)$ $9.6\,h^{-1}$ Mpc simulations agree well in the b-distribution, but disagree with the $(N_{\rm p}, N_{\rm g}) = (256, 256)$ simulations. It would appear that AUTOVP is picking up unreal features resulting from noise in the $N_{\rm p} = 128$ simulations that decrease in going to $N_{\rm p} = 256$. Increasing the grid resolution, holding $N_{\rm p} = 256$ fixed, however, appears to recover real features that correspond statistically to the previously unresolved fluctuations in the $(N_{\rm p}, N_{\rm g}) = (128, 256)$ simulations. Since the same trend is found for the wavelet coefficients, it seems unlikely that the non-monotonic behaviour is an artefact of the line finding and fitting procedures used by AUTOVP. There are no obvious systematic trends with box size; the results otherwise appear to have converged to better than 5 per cent.

Also shown are the results for HPM for the $9.6\,h^{-1}$ Mpc box and $(N_{\rm p}, N_{\rm g}) = (256, 512)$. Both the column density distribution and the Doppler parameter distribution agree well with the $N_{\rm p} = N_{\rm g} = 256$

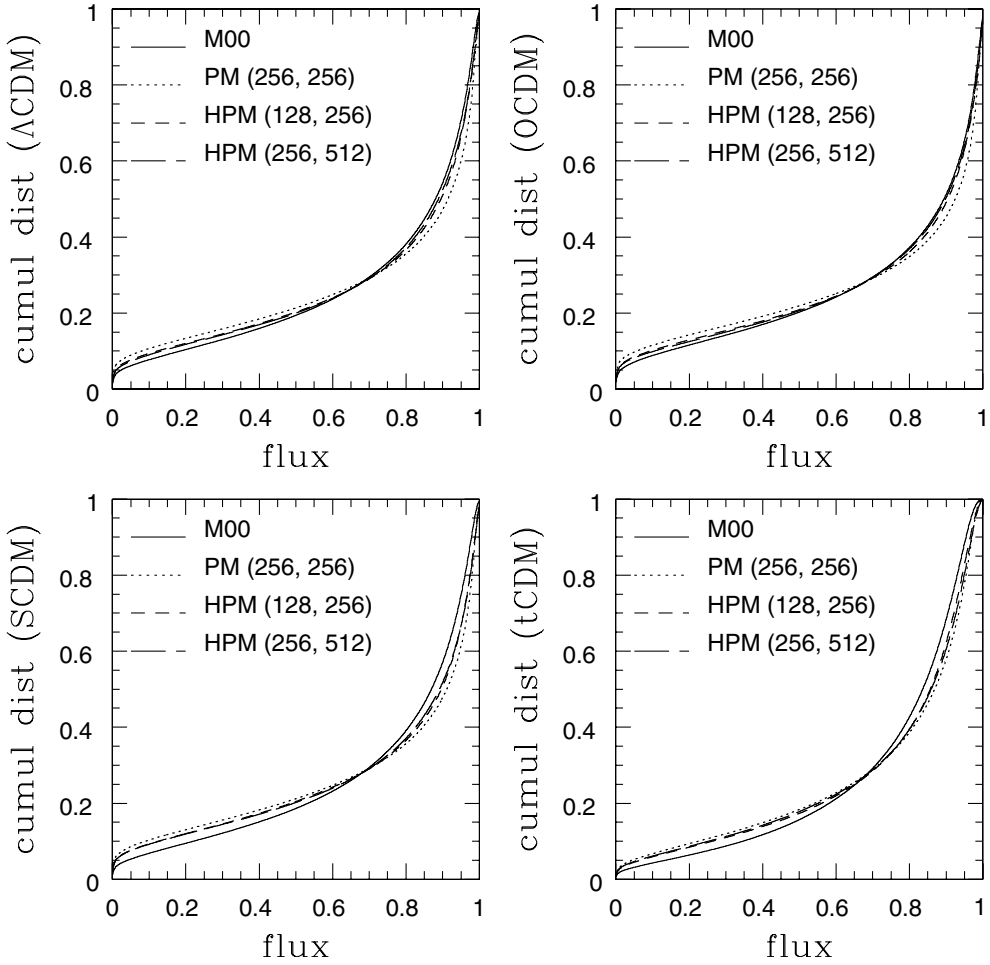

Figure 7. Comparison of cumulative distributions of flux per pixel for four cosmological models corresponding to the box sizes in M00. The particle and grid numbers are shown as $(N_{\rm p}, N_{\rm g})$.

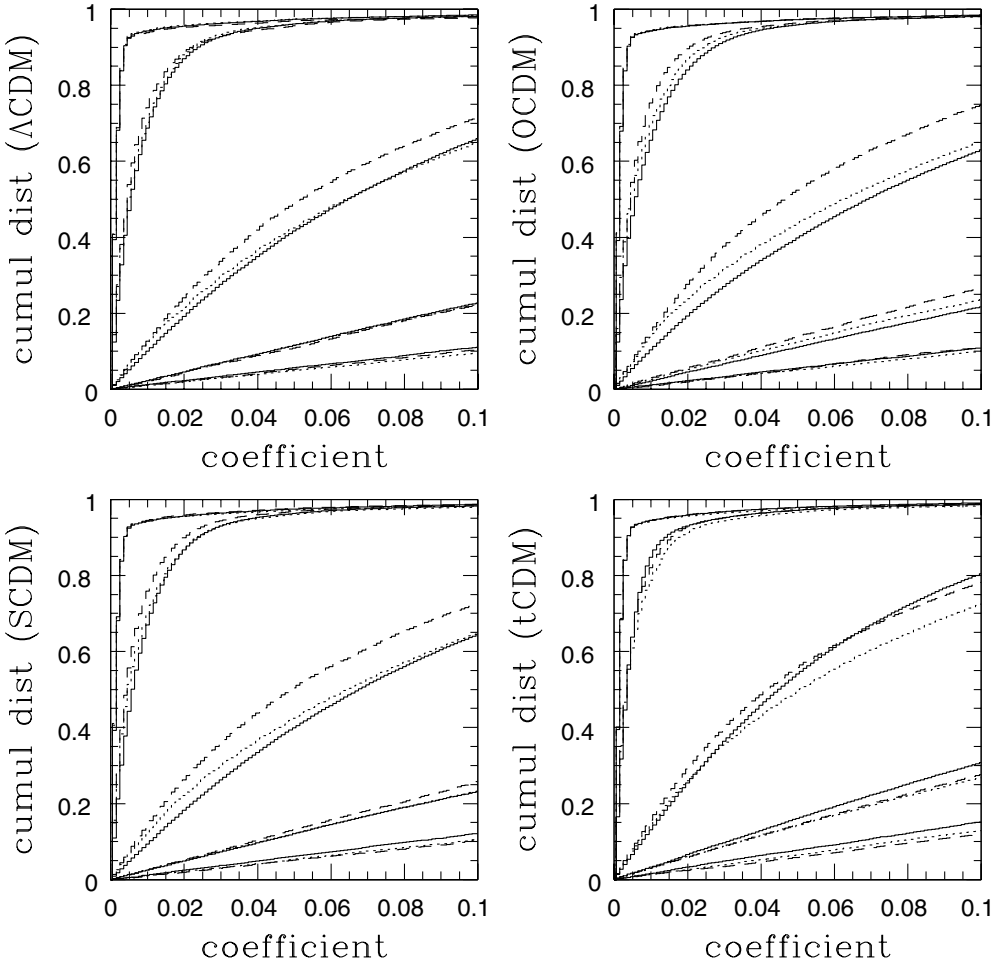

Figure 8. Comparison of wavelet coefficient distributions for PM, HPM, and the simulations of M00 (continuous lines). The PM results are shown for $N_{\rm p} = N_{\rm g} = 256$ (dotted lines) and the HPM results for $N_{\rm p} = 128$, $N_{\rm g} = 256$ (dashed lines). The groups of coefficient distributions are ordered as in Fig. 4.

$9.6\,h^{-1}$ Mpc PM simulation, demonstrating that incorporating the pseudo-pressure forces in the HPM simulation has very little effect on the resulting absorption line parameter distributions for this model. We note that the HPM simulation tends to produce distributions shifted somewhat to higher column density and Doppler parameter compared with the analogous $(N_{\rm p}, N_{\rm g}) = (256, 512)$ PM simulation.

A comparison of the results for HPM for different box sizes and particle/grid numbers is shown in Fig. 6. The $N_{\rm H\,I}$ distributions are well-converged. The *b*-distributions would have appeared to converge, except the distributions shift toward larger *b*-values in the highest resolution small box simulation. Curiously, this is opposite to the trends reported in the resolution studies of Theuns et al. (1998a,b) and Bryan et al. (1999), who found that the *b*-values tended to decrease with both decreasing box size and increasing resolution, although at lower resolutions compared with our simulations. The trends found in the full hydrodynamics simulations are physically sensible: a larger box adds longer wavelength power to the simulations, which may increase the peculiar velocities of the dark matter and the gas, while higher particle and grid numbers permit higher resolution of density fluctuations and shocks, which may result in a narrowing of absorption features. Possibly the opposing trend found here is a consequence of not allowing for shocks. For a typical sound speed of $\sim 10\,{\rm km\,s^{-1}}$ and peculiar velocities in the gas of $\sim 100\,{\rm km\,s^{-1}}$,

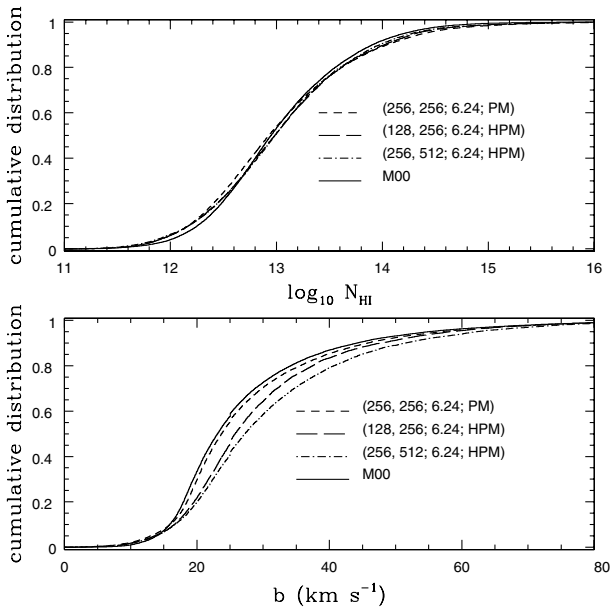

Figure 9. Comparison of line parameter distributions for PM, HPM, and the simulations of M00 for ΛCDM.

shocks may be expected to play an important role in the velocity structure of the lines.

4 COMPARISON WITH HYDRODYNAMICAL SIMULATIONS

In this section, we compare the results of the PM and HPM simulations against the Kronus simulation results of M00 for a variety of cosmological models. The simulations were run for the same cosmological models as in M00, matching the box sizes and the numbers of hydrodynamical cells and grid points for the gravitational force calculations.

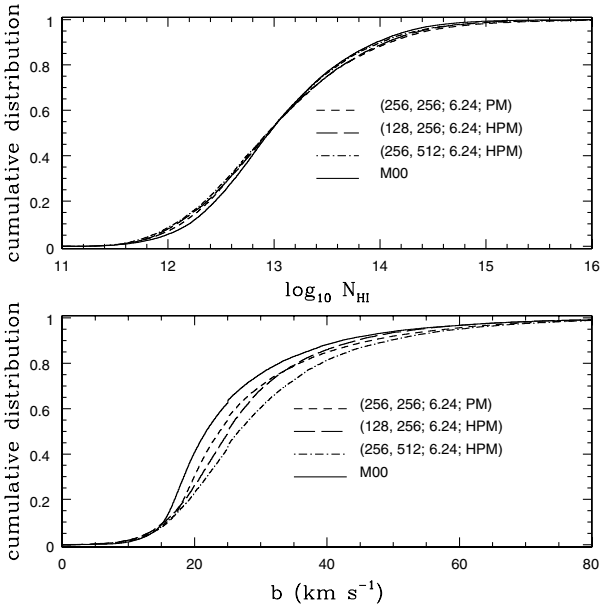

Figure 10. Comparison of line parameter distributions for PM, HPM, and the simulations of M00 for OCDM.

4.1 Flux distribution

The distributions of flux for the four cosmological models considered are shown in Fig. 7. Excellent agreement is found between HPM and the full hydrodynamical simulations (M00), with the agreement being least good for SCDM. The agreement with PM is not as good, but the cumulative distributions still agree within 10 per cent. The agreement between both sets of $N_{\rm p}$ and $N_{\rm g}$ pairs for the HPM simulations shows that the results have converged at the relevant box sizes.

4.2 Wavelet decomposition

The cumulative distributions for the wavelet coefficients are shown in Fig. 8. A much better agreement is generally found between the PM simulations and the full hydrodynamical simulations than is found for HPM. The agreement is even poorer for the HPM simulations with $(N_{\rm p}, N_{\rm g}) = (256, 512)$ in all cases. The smaller values for the coefficients in the HPM spectrum indicate that the artificial hydrodynamics in HPM suppresses the full amount of velocity structure in the spectra compared with that found in the full hydrodynamics calculations.

4.3 Line parameter decomposition

The results of the Voigt line parameter analyses using AUTOVP are shown in Figs 9–12. Both the PM and HPM results agree reasonably well with the results of M00 for the H I column density distributions. The best agreement for the Doppler parameter distributions is found for the PM simulations: the HPM simulations produce features that are too broad. While the PM and HPM simulations agree with the results of M00 to 5–10 per cent on the $N_{\rm H\,I}$ distributions, the agreement between the Doppler parameter distributions is worse: ~10 per cent for PM and ~20 per cent for HPM. The disagreement between the Doppler

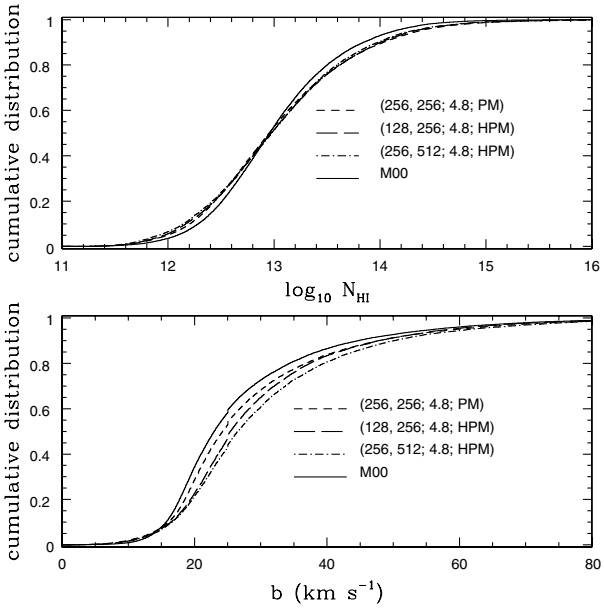

Figure 11. Comparison of line parameter distributions for PM, HPM, and the simulations of M00 for SCDM.

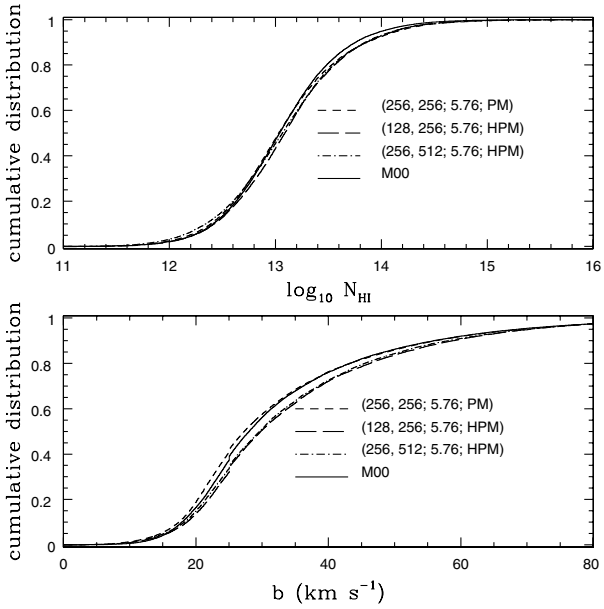

Figure 12. Comparison of line parameter distributions for PM, HPM, and the simulations of M00 for tCDM.

parameter distributions tends to increase with the magnitude of the power spectra at $z = 3$.

5 SUMMARY

We have performed several simulations of the Lyα forest using different background cosmological models, numerical codes and grid resolutions. Convergence to the distributions of flux, wavelet coefficients, and absorption line parameters tends to be non-monotonic for the PM simulations as the number of particles and grid zones is increased, although agreements in the cumulative distributions to within 10 per cent are achieved.

A comparison with full hydrodynamical calculations shows that there is little advantage in HPM over PM, except possibly for the flux distributions. The HPM simulations generally result in broader absorption lines than PM. Both the PM and HPM simulations tend to yield broader lines than found in the full hydrodynamics calculations. This may be a consequence of the neglect of shocks in the PM and HPM simulations, which may sharpen the velocity structure of the absorption lines.

The simulations show that the principal spectral properties of the Lyα forest may be qualitatively reproduced from the dark matter structures alone, to a remarkable accuracy of 10 per cent in the cumulative distributions of flux, wavelet coefficients, H I column density, and Doppler parameter. Tests of the models, however, require agreement at the 5 per cent level per spectrum or better at the resolution of the Keck HIRES (Meiksin et al. 2001), so that ultimately full hydrodynamical calculations will be required to confront models for the structure and physical properties of the Lyα forest with direct observations. In order to match the observed spectra, it may ultimately be necessary to incorporate radiative transfer into the simulations, both to allow for spatial fluctuations in the UV ionizing background and to reproduce the correct gas temperatures (and linewidths), particularly if helium is completely photoionized at only moderate redshifts. Several other physical effects may also be important, such as heating sources in addition to QSOs or galactic feedback like winds. Although it is not yet possible to test the accuracy of the PM simulations in the presence of these effects, our results suggest that, at least when hydrodynamics is not dominant, the PM simulations alone may be of adequate accuracy for investigating some of these issues without requiring the considerable overhead of solving the full set of hydrodynamics equations.

ACKNOWLEDGMENTS

The authors thank G. Bryan for permission to use the results of his Kronos simulations, and R. Davé for permission to use AUTOVP. MW was supported by the US National Science Foundation and a Sloan Fellowship. Parts of this work were done on the Origin2000 system at the National Center for Supercomputing Applications, University of Illinois, Urbana-Champaign.

REFERENCES

Bardeen J. M., Bond J. R., Kaiser N., Szalay A. S., 1986, ApJ, 304, 15
Bond J. R., Wadsley J. W., 1997, in Petitjean P., Charlot S., eds, Structure and Evolution of the Intergalactic Medium from QSO Absorption Line Systems. Editions Frontières, Paris, p. 143
Bryan G. L., Machacek M., Anninos P., Norman M. L., 1999, ApJ, 517, 13
Bunn E. F., White M., 1997, ApJ, 480, 6
Cen R., Miralda-Escudé J., Ostriker J. P., Rauch M., 1994, ApJ, 437, L9
Croft R. A. C., Weinberg D. H., Katz N., Hernquist L., 1998, ApJ, 495, 44
Davé R., Hernquist L., Weinberg D. H., Katz N., 1997, ApJ, 477, 21
Gnedin N. Y., Hui L., 1998, MNRAS, 296, 44
Hernquist L., Katz N., Weinberg D., Miralda-Escudé J., 1996, ApJ, 457, L51
Hockney R. W., Eastwood J. W., 1988, Computer Simulation Using Particles. Adam Hilger, Bristol
Hui L., Gnedin N. Y., 1997, MNRAS, 292, 27
Machacek M. E., Bryan G. L., Meiksin A., Anninos P., Thayer D., Norman M. L., Zhang Y., 2000, ApJ, 532, 118 (M00)
Meiksin A., 1994, ApJ, 431, 109
Meiksin A., 2000, MNRAS, 314, 566
Meiksin A., White M., Peacock J. A., 1999, MNRAS, 304, 851
Meiksin A., Bryan G. L., Machacek M. E., 2001, MNRAS, submitted
Petitjean P., Mücket J. P., Kates R. E., 1995, A&A, 295, L9
Theuns T., Leonard A., Efstathiou G., 1998a, MNRAS, 297, L49
Theuns T., Leonard A., Efstathiou G., Pearce F. R., Thomas P. A., 1998b, MNRAS, 301, 478
White M., 1999, MNRAS, 310, 511
Zhang Y., Anninos P., Norman M. L., 1995, ApJ, 453, L57
Zhang Y., Anninos P., Norman M. L., Meiksin A., 1997, ApJ, 485, 496
Zhang Y., Meiksin A., Anninos P., Norman M. L., 1998, ApJ, 495, 63

This paper has been typeset from a TEX/LATEX file prepared by the author.